2020

The variable resonance magnetorheological pendulum tuned mass damper: Mathematical modelling and seismic experimental studies

Matthew Christie
University of Wollongong, mdc769@uowmail.edu.au

Shuaishuai Sun
University of Wollongong, ssun@uow.edu.au

Lei Deng
University of Wollongong, ld530@uowmail.edu.au

Donghong Ning
University of Wollongong, dning@uow.edu.au

Haiping Du
University of Wollongong, hdu@uow.edu.au

See next page for additional authors

The variable resonance magnetorheological pendulum tuned mass damper: Mathematical modelling and seismic experimental studies

Abstract

Tuned mass damper technologies are progressively advancing through innovative application of smart materials, facilitating more versatile infrastructure protection. During seismic events, primarily encountered surrounding fault lines, highrise buildings and other civil structures can suffer catastrophic failures if not adequately protected. Where traditional passive structural protection may mitigate such damage, adaptive systems which provide controllable vibration attenuation across a wide range of excitation frequencies have seen growth in use, overcoming the challenges resulting from unpredictable seismic spectrums. As a robust solution to this problem, this article presents and analyses a variable resonance magnetorheological-fluid-based pendulum tuned mass damper which employs a rotary magnetorheological damper in a controllable differential transmission to add stiffness to a swinging pendulum mass. The device is mathematically modelled based on magnetic field analysis, the Bingham plastic shear-stress model for magnetorheological fluids, and planetary gearbox kinematic and torque relationships, with the model then being validated against experimental data. The passive and semi-active-controlled performance of the device in seismic vibration suppression is then experimentally investigated using a scale five-storey building. In tests conducted with the 1985 Mexico City record, the semi-active device outperformed the (optimal) passive-on tuning, at best reducing peak displacement by 15.47% and acceleration by 28.28%, with similar improvement seen against the passive-off case for the 1940 El Centro record.

Disciplines

Engineering | Science and Technology Studies

Publication Details

Christie, M. D., Sun, S., Deng, L., Ning, D., Du, H., Zhang, S. & Li, W. (2020). The variable resonance magnetorheological pendulum tuned mass damper: Mathematical modelling and seismic experimental studies. Journal Of Intelligent Material Systems And Structures, 31 (2), 263-276.

Authors

Matthew Christie, Shuaishuai Sun, Lei Deng, Donghong Ning, Haiping Du, Shiwu Zhang, and Weihua Li

The Variable Resonance Magnetorheological Pendulum Tuned Mass Damper: Mathematical Modelling and Seismic Experimental Studies

M. D. Christie[1], S. Sun[*1], L. Deng[1], D. H. Ning[2], H. Du[2], S. W. Zhang[*3] and W. H. Li[1]

[1]School of Mechanical, Materials, Mechatronic, and Biomedical Engineering, University of Wollongong, New South Wales 2522, Australia

[2]School of Electrical, Computer & Telecommunications Engineering, University of Wollongong, New South Wales 2522, Australia

[3]Department of Precision Machinery and Precision Instrumentation, University of Science and Technology of China, Hefei, Anhui province 230026, China

[*]Corresponding author emails: ssun@uow.edu.au; swzhang@ustc.edu.cn

Abstract

Tuned mass damper technologies are progressively advancing through innovative application of smart materials, facilitating more versatile infrastructure protection. During seismic events, primarily encountered surrounding fault lines, high-rise buildings and other civil structures can suffer catastrophic failures if not adequately protected. Where traditional passive structural protection may mitigate such damage, adaptive systems which provide controllable vibration attenuation across a wide range of excitation frequencies have seen growth in use, overcoming the challenges resulting from unpredictable seismic spectrums. As a robust solution to this problem, this paper presents and analyses a variable resonance magnetorheological-fluid-based pendulum tuned mass damper which employs a rotary magnetorheological damper in a controllable differential-transmission to add stiffness to a swinging pendulum mass. The device is mathematically modelled based on magnetic field analysis, the Bingham plastic shear-stress model for magnetorheological fluids, and planetary gearbox kinematic and torque relationships, with the model then being validated against experimental data. The passive and semi-active-controlled performance of the device in seismic vibration suppression is then experimentally investigated using a scale 5-story building. In tests conducted with the 1985 Mexico City record, the semi-active device outperformed the (optimal) passive-on tuning, at best reducing peak displacement by 15.47% and acceleration by 28.28%, with similar improvement seen against the passive-off case for the 1940 El Centro record.

Keywords: magnetorheological fluid, building protection, vibration absorber, tuned mass damper, differential, mathematical modelling

1. Introduction

Civil structures including: bridges, highways, and high-rise buildings are often a point of focus for oversite to include seismic protection when building in regions with nearby fault lines or a history of seismic activity (Fisco and Adeli, 2011; Gutierrez Soto and Adeli, 2013). Although smaller-scale infrastructure may also succumb to seismic events, the catastrophic failures that occur when these megastructures suffer significant damage gives reason to a greater effort to protect them against ground vibration. For high-rise buildings, it is common-place to see either base isolation or tuned mass dampers employed to control and attenuate earthquake-induced vibration (Fisco and Adeli, 2011). Where these two methods differ is in the working mechanisms; base isolation serves to reduce the transmissibility of earthquakes to the protected structure by essentially 'de-coupling' the building from the source of the excitation (Yang et al., 2016; Buckle and Mayes, 1990). On the other hand, tuned mass dampers (TMDs) are energy absorption and dissipation devices which are placed inside the structure to attenuate the vibration (Gutierrez Soto and Adeli, 2013), also making them useful in suppressing wind-induced building sway.

The way in which these tuned mass dampers attenuate the vibration of the megastructure is through appropriate tuning, such that the device possesses a resonant frequency similar to that of the structure they are placed in (Hoang, 2008). While passive TMDs with a fixed resonant frequency have commonly seen implantation in buildings, innovations have led to various designs and mechanisms which facilitate controllable and adaptive tuning solutions to provide greater absorption bandwidth and hence improved performance. For a tuned liquid-column damper (TLCD) holding specific volumes of a water-based liquid in tanks to absorb vibration energy, controllable valves and movable panels have been employed to shift TMD resonance through augmenting flow behaviour (Altay and Klinkel, 2018). It has also been reported, the idea of controllable pendulum length using winch-driven support cables in pendulum tuned mass dampers (PTMDs), providing adjustable oscillation period and hence resonant frequency (Lourenco, 2011). For the more conventional shear-mode tuned mass dampers, effectively a mass resting on a bearing, coupled to the building through some stiffness and damping, these have seen relatively wide-spread implementation of controllable resonance through the application of smart materials with controllable mechanical properties (Kela, 2009; Sun et al., 2015).

The benefit and in some cases necessity of variable resonance in tuned mass dampers is the ability to track the frequency of ground excitation and adjust the TMD resonance in real-time to provide enhanced vibration absorption for earthquakes with unpredictable or shifting dominant

frequencies (Zhang and Wang, 2013). For a passive tuned mass damper with limited absorption bandwidth, vibration attenuation will only occur optimally at the resonance of the building, causing exacerbated vibration for earthquakes of dominant frequencies surrounding this operation point (Sun et al., 2018). For adaptively tuned TMDs, commonly referred to as adaptive tuned vibration absorbers (ATVAs), through quite simple acceleration feedback, short time Fourier transform (STFT) is often applied as a means of measuring the real-time frequency of the ground excitation to the building. To then set the resonance of the TMD to match this frequency for effective absorption, actuators may be employed to provide some form of active control, however a more robust and reliable approach (Arash Yeganeh and Touraj, 2014) is to adjust the mechanical properties of the TMD to shift the resonance, this being what is known as semi-active control.

In any case for TMD resonance control, active or semi-active, a requirement for optimal performance is a fast response. Where, for example, a controllable length PTMD may require time in the order of seconds to adjust its resonant frequency, smart materials exist which can offer a near-instantaneous change in mechanical properties. Magnetorheological (MR) materials are an ideal candidate for this application as they offer controllable stiffness and damping with a response in the order of milliseconds (de Vicente, 2011), in the case of MR elastomer (MRE) and MR fluid (MRF), respectively. MR materials possess changeable rheological properties which respond to the stimulus of a magnetic field. When in proximity, the magnetic field causes alignment of suspended micro-scale iron particles, hosted in an elastomeric matrix, i.e. MRE, or host fluid, i.e. MRF, resulting in the aforementioned controllable stiffness and damping. This behaviour has led to MR materials seeing wide-spread use in various fields where vibration is a key issue for performance and safety, such as vehicle dynamics (Tang, 2017; Sun et al., 2015; Harris et al., 2017), manufacture (Jha and Jain, 2004; Jain, 2008; Yao et al., 2011), and seismic vibration control (Zhou et al., 2010; Sun et al., 2018; Christie et al., 2019). Although MRE has been demonstrated to be effective in facilitating variable resonance in tuned mass dampers before, stroke limitations and possible yielding of the material inspired the authors of this paper to employ MRF to accomplish this in a more robust way without such limitations.

MR fluid on its own can only provide variable damping, unlike MR elastomer which can easily facilitate variable resonance in a TMD as its stiffness can directly be controlled. For this reason, this work presents the magnetorheological pendulum tuned mass damper (MR-PTMD), which employs a rotary MR damper controlled differential transmission, governing the overall stiffness of the device by controlling the level of engagement of an included mechanical spring.

This innovative application of a planetary gearbox provides a novel, yet effective means of coupling these components with the pendulum mass to provide a variable resonance TMD. To analytically investigate the working of the device, first experimentally characterised in the authors' previous work (Christie et al., 2019), a mathematical model describing the device is derived and experimentally validated in this paper, with a controller based on short-time Fourier transform (STFT) presented. Further experimental scale-building seismic case-studies are then carried-out to observe the performance of the device with records of varied frequency spectrums, in particular the 1940 El Centro and 1985 Mexico City earthquakes.

The remainder of the paper takes on the following structure. Section 2 includes the design, magnetic field study, and discusses the working mechanism of the MR-PTMD. Section 3 describes the mathematical modelling, model validation, and controller design of the device. Section 4 details the experimental performance of the device in scale-building tests under seismic excitation for two earthquake records. Conclusions are lastly discussed in Section 5.

2. Design and Working Mechanism of the MR-PTMD

2.1. MR-PTMD Structure

Illustrated in **Figure 1**, the prototype MR-PTMD has been modelled using CAD software to aid the design process. For brevity, details of this process and the basis of selection for parameters such as TMD mass and pendulum length can be found in (Christie et al., 2019). Nevertheless, as shown, the device includes a frame mass m_a of 3.2 kg, and a pendulum mass m_p of 1.75 kg, suspended a length l_p from its rotational axis of 70 mm in a mass hanger of negligible mass. Focusing on the right of the diagram, the included torsional spring with a stiffness k_t of 1.67 N·m/rad is coupled through the planetary gearbox to the pendulum mass, with the degree of power transmission from one to the other governed by the braking-torque of the rotary MR damper on the left side of the device. The frame of the device is constructed from aluminium extrusion, with the supports and mass hanger being 3D printed Nylon plastic. The remaining components, including the pendulum mass, spring, and much of the damper, are various grades of steel.

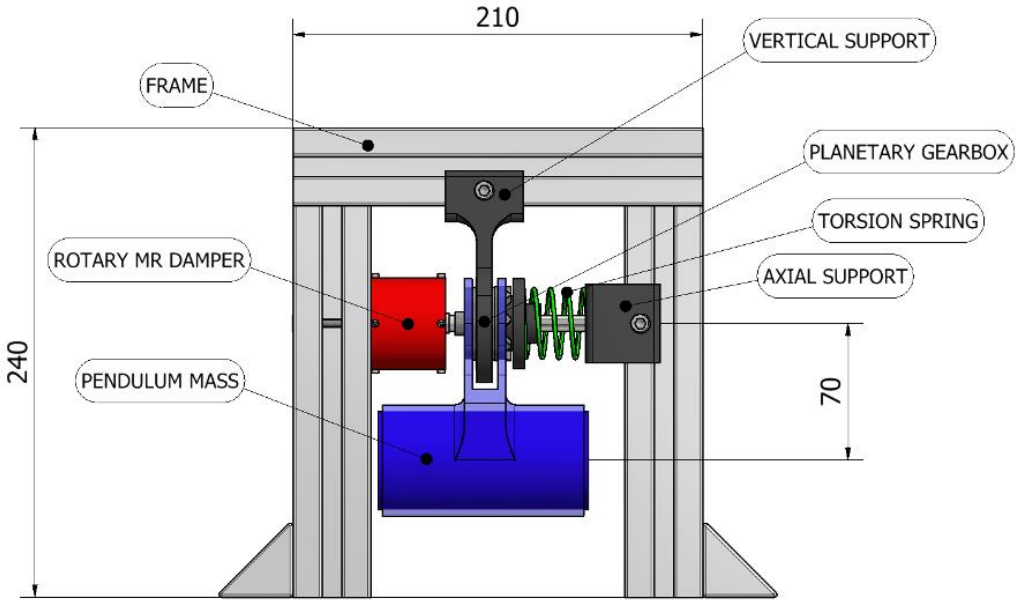

Figure 1 – MR-PTMD prototype CAD model (dims in mm)

2.2. Rotary MR Damper Structure and Torque Modelling

A key part of the device, the rotary MR damper enables the variable resonance behaviour and is detailed in the CAD model shown in **Figure 2**. The main guidelines that shaped the device were a high torque density and efficient magnetic field generation. The body length of the damper is 38 mm, with shaft extensions not making it much larger, and the major diameter is 47 mm. The shaft inside is aluminium to reduce mass, with the yoke and rotor being machined out of low carbon steel to provide high magnetic permeability to reduce the effects of magnetic saturation. To supply the magnetic flux through the MRF (MRF-140CG, produced by LORD Corp.) to increase damping torque, this flux indicated by the red loops of the figure, a set of electromagnetic coils of 120 turns each was used. With no current, the low viscosity of the MRF allows relative motion between the inside aluminium shaft and the outside low carbon steel yoke, however this motion becomes increasingly restricted as current supplied to these coils and hence the induced magnetic field is increased.

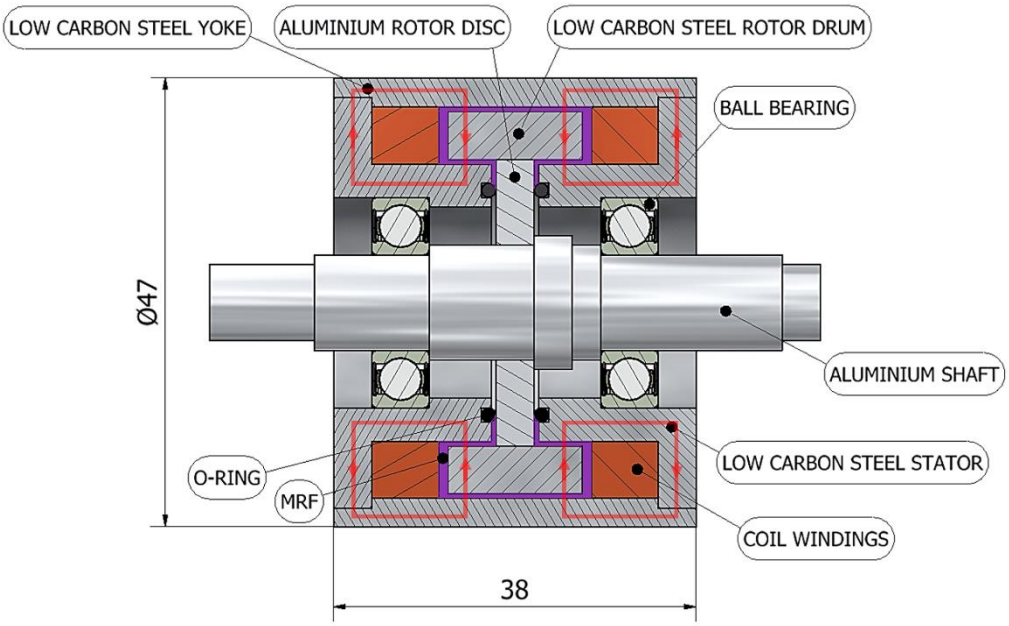

Figure 2 – Rotary MR damper schematic (dims in mm)

To assist with the design of the damper and build a mathematical description of its current-input to torque-output behaviour, material data for the LORD MRF-140CG used (Co., 2008) was considered in conjunction with stationary magnetic field modelling in COMSOL Multiphysics ver. 5.1, illustrated in **Figure 3(b)**. Within the simulation, the B-H curve from the manufacture data was employed for the MRF, with common materials defined using default software parameters. From the plotted results in **Figure 3(a)**, it can be seen that the maximum axial-mean flux density induced in the inner gap of the damper B_i is 1.184 T under 3 A current to the coils, with that of the outer gap B_o being recorded as 0.637 T.

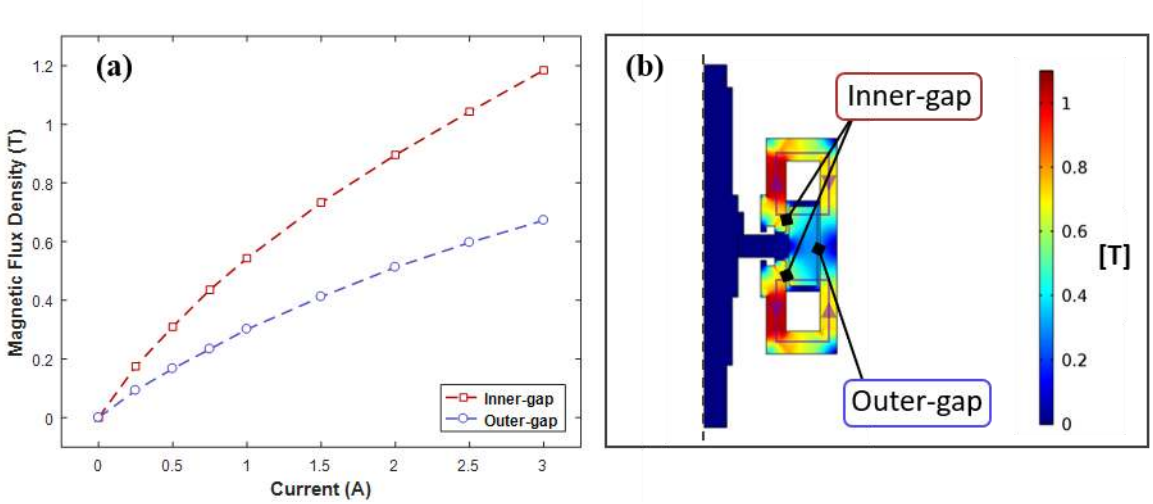

Figure 3 – Magnetic field FEM analysis: (a) mean flux through MRF, (b) joint model

From the simulation result provided in **Figure 3(a)**, the axial-mean flux through the inner and outer gaps of the MR damper, B_i and B_o respectively, can be identically approximated by the following quadratic equations within a 0 to 3 A input current I range. First, the inner flux:

$$B_i(I) = -0.0636I^2 + 0.5709I \quad [\text{T}], \tag{1}$$

and then the outer flux:

$$B_o(I) = -0.0385I^2 + 0.3311I \quad [\text{T}]. \tag{2}$$

Following the B-H curve for the MRF, as applied in the simulation study, the magnetic field strength H can be described as a function of flux density B:

$$H(B) = 60.7433B^3 + 105.8471B^2 + 33.5748B \quad [\text{kA/m}]. \tag{3}$$

Also using manufacturer data as a guideline, the relationship between the shear yield stress τ_y and field strength H is:

$$\tau_y(H) = -0.7980H^2 + 323.3040H + 3439.95 \quad [\text{Pa}]. \tag{4}$$

To convert this stress into a post-yield output torque $T_{MR,y}$ for the damper, considering a Bingham plastic model, this is the sum of two components, a Coulomb friction torque T_C, and a viscous rate-dependent damping torque T_η, i.e. $T_{MR,y} = T_C + T_\eta$ (Imaduddin et al., 2013). Assuming T_η to be relatively insignificant in the post-yield state, which is reasonable given the TMD operational frequency range, we may neglect the viscous-damping term and describe the joint torque through the following:

$$\begin{aligned} T_{MR,y} = T_C(\tau_y) &= 2\pi\left(\tau_{y,i}(H_i) \times w_i \times r_i^2 + \tau_{y,o}(H_o) \times w_o \times r_o^2\right) \\ &= 2\pi\left(\tau_{y,i}(H_i) \times 0.01 \times 0.015^2 + \tau_{y,o}(H_o) \times 0.014 \times 0.02^2\right) \quad [\text{N} \cdot \text{m}], \end{aligned} \tag{5}$$

where w and r are the axial lengths and radii, respectively, of the inner and outer drum areas of the rotary damper. Given **Equations 1 and 2** are functions of coil input current I, **Equation 5** therefore describes the damper's current-torque relationship.

2.3. MR-PTMD Working Mechanism

As presented, through supply of electric current of up to 3 A to the coils of the MR damper included in the MR-PTMD, the controllable magnetic field provides a variable damping torque, governed by **Equation 5**. With this damper being connected to one of the three ports of a planetary gearbox (planet carrier), illustrated in **Figure 4**, the control of this torque has a governing effect on the other two ports of the gearbox. These remaining two ports connect to a pendulum mass m_p through an arm of length l_p from the rotational axis (ring gear), and a torsional spring of stiffness k_t (sun gear). Under a translational displacement x_a (relative to ground), the pendulum mass rotates an angle θ_p which serves as an input to the system. Through the gearbox, this then leads to rotations of the MR damper and torsional spring of θ_{MR} and θ_k, respectively. In the extreme case of when the damper is sufficiently powered to lock with a high braking torque, the damper will be fixed and the spring will be caused to rotate (i.e. $\Delta\theta_{MR} \cong 0$ and $\Delta\theta_k \neq 0$), and when it is not powered, the damper will rotate easily with very little spring motion (i.e. $\Delta\theta_{MR} \neq 0$ and $\Delta\theta_k \cong 0$). The behaviour for any control case of the device is identical to this, with these two cases representing pre-yield and post-yield damper states, respectively.

The transfer of motion from the pendulum mass θ_p to the damper and spring, θ_{MR} and θ_k, respectively, is governed through the torque balance across the two outputs of the gearbox (taking the pendulum mass connected to the ring gear as input). This motion can be described by both, the kinematic relationship:

$$0 = \theta_p + \theta_k \frac{N_S}{N_R} - \theta_{MR}\left(\frac{N_R + N_S}{N_R}\right), \tag{6}$$

where $N_S = 9$ and $N_R = 41$ are the number of gear teeth of the sun and ring gears, respectively, and the internal torque balance of the gearbox:

$$T_k\left(\frac{N_R}{N_S}\right) = T_{MR}\left(\frac{N_R}{N_R + N_S}\right), \tag{7}$$

where T_k is the output torque from the spring, and T_{MR} is the output torque from the damper, which will become $T_{MR,y}$ in the post-yield state, n.b. the teeth ratios are arranged such that the torque comparison is from the perspective of the common pendulum mass. From **Equation 6**, we can consider the two cases: (1) the pre-yield case, when the damper can be considered fixed, and

(2) the post-yield case, when the spring can be considered fixed. For the first, pre-yield, case, the angular displacement of the spring θ_k can be conveniently taken as:

$$\theta_k = -\left(\theta_p + \theta_{p,y} - \theta_{p,max}\right)\left(\frac{N_R}{N_S}\right), \tag{8}$$

where $\theta_{p,y}$ and $\theta_{p,max}$ are respectively the pendulum angle at which the damper will yield, entering the post-yield state, and the maximum pendulum angle, at which the pendulum's velocity $\dot{\theta}_p$ will change direction, returning the damper to the pre-yield state. As for the second, post-yield, case, the angular displacement of the MR damper θ_{MR} can be described by:

$$\theta_{MR} = \left(\theta_p - \theta_{p,y} + \theta_{p,y-old}\right)\left(\frac{N_R}{N_R + N_S}\right), \tag{9}$$

where $\theta_{p,y}$ and $\theta_{p,y-old}$ are the pendulum yield angles for the current and previous states, respectively.

It should be noted, **Equations 8 and 9** are valid only when in the pre-yield and post-yield states, respectively, with these assumed to be constant when not in the appropriate state. From **Equation 7**, we can generate the necessary conditions for the pre- and post-yield states of the damper by considering this when solved for T_{MR}. For the pre-yield state, the damping torque T_{MR}, balanced by the ratio-attached spring torque T_k, must be strictly less than the yielding toque $T_{MR,y}$ for any given solenoid current and hence applied magnetic field. So, the condition may be written as $|T_{MR}| \leq T_{MR,y}$ for the pre-yield case where the gearbox output torque to the pendulum mass $T_{GB} = T_k(N_R/N_S)$, and then $|T_{MR}| > T_{MR,y}$ for the post-yield case with $T_{GB} = T_{MR,y}(N_R/(N_R + N_S))$. Given the nature of the loading of the damper, to return to the pre-yield state from the post-yield state, the pendulum's velocity would need to become zero or change direction. In addition to the induced torques in either case, the device also includes a relatively small amount of internal damping c_{GB} associated with gear-mesh efficiency, which is defined as 0.015 N·m·s/rad in later simulation studies, consistent with observed prototype behaviour.

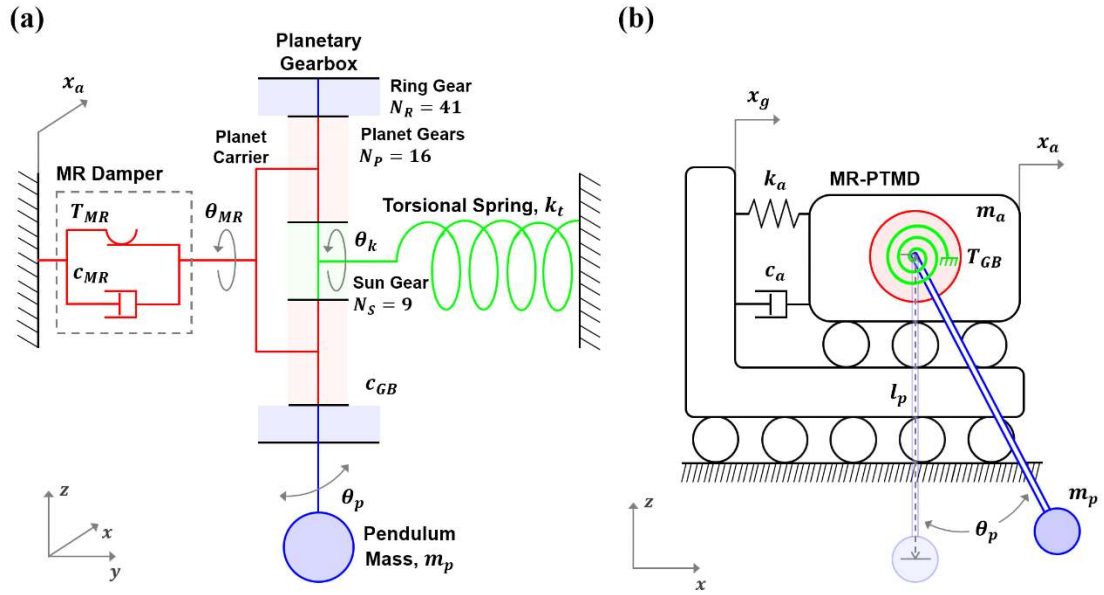

Figure 4 – MR-PTMD schematic diagram: (a) front view, and (b) side view

3. Mathematical Modelling and Control of the MR-PTMD

3.1. Model Derivation

With reference to the coordinates and parameters of the MR-PTMD system detailed in **Figure 4**, the system can be modelled following the Euler-Lagrange formulation for classical mechanics. In this approach, the balance of kinetic energy T and potential energy V is the focus, and for a non-conservative system such as this, the model must also be inclusive of the Rayleigh dissipation function for viscous damping D. The form the Euler-Lagrange equation then takes is:

$$\frac{d}{dt}\left(\frac{\partial L}{\partial \dot{q}_i}\right) - \frac{\partial L}{\partial q_i} + \frac{\partial D}{\partial \dot{q}_i} = Q_i, \tag{10}$$

where $L = T - V$ is the Lagrangian, q_i is the i^{th} generalised coordinate, and Q_i is the i^{th} generalised force. For the MR-PTMD, we may take $q_1 = x_a$, where x_a is displacement relative to ground and $q_2 = \theta_p$ as the relevant coordinates, with $Q_1 = -\ddot{x}_g(m_a + m_p)$ and $Q_2 = -\ddot{x}_g m_p l_p$ as the external forces acting on the system.

Now, the energies of the system may be considered; the kinetic energy T is given by:

$$T = \frac{1}{2}(m_a + m_p)\dot{x}_a^2 + m_p l_p \dot{x}_a \dot{\theta}_p \cos(\theta_p) + \frac{1}{2} m_p l_p^2 \dot{\theta}_p^2, \tag{11}$$

the potential energy V is defined as:

$$V = T_{MR,y}\,\mathrm{sgn}\left(\dot{\theta}_{MR}\right)\theta_{MR} + \frac{1}{2}k_t\theta_k^2 + m_p g l_p\left(1-\cos\left(\theta_p\right)\right) + \frac{1}{2}k_a x_a^2,$$

where $T_{MR,y}\mathrm{sgn}\left(\dot{\theta}_{MR}\right)\theta_{MR}$ is the generalised potential of the Coulomb friction component of the MR damper. This equation must be manipulated further, however, putting both θ_{MR} and θ_k in terms of the pendulum angle θ_p. From **Equations 8 and 9**, we can obtain a more useful, however conditional, description of this potential energy V:

$$\begin{aligned} V = {} & T_{MR,y}\,\mathrm{sgn}\left(\dot{\theta}_p\right)\left(\frac{N_R}{N_R+N_S}\right)\left(\theta_p - \theta_{p,y} + \theta_{p,y-old}\right) \\ & + \frac{1}{2}k_t\left(\theta_p + \theta_{p,y} - \theta_{p,max}\right)^2\left(\frac{N_R}{N_S}\right)^2 \\ & + m_p g l_p\left(1-\cos\left(\theta_p\right)\right) + \frac{1}{2}k_a x_a^2. \end{aligned} \tag{12}$$

Lastly, the Rayleigh dissipation function for viscous damping D, neglecting that of the MR damper c_{MR}, which has been considered negligible relative to the Coulomb friction component $T_{MR,y}$, simplifies to:

$$D = \frac{1}{2}c_a\dot{x}_a^2 + \frac{1}{2}c_{GB}\dot{\theta}_p^2, \tag{13}$$

where c_{GB} is the friction-induced energy loss through the planetary gearbox transmission.

Evaluating the Euler-Lagrange equation, **Equation 10**, for each set of coordinates and forces when making use of **Equations 11-13,** leads to the set of non-linear equations describing the system. For $q_1 = x_a$:

$$\begin{aligned} & \left(m_a + m_p\right)\ddot{x}_\mathrm{a} + m_p l_p\ddot{\theta}_p\cos\left(\theta_p\right) - m_p l_p\dot{\theta}_p^2\sin\left(\theta_p\right) + c_a\dot{x}_a + k_a x_a \\ & \qquad = -\ddot{x}_g\left(m_a + m_p\right), \end{aligned} \tag{14}$$

for $q_2 = \theta_p$:

$$m_p l_p\ddot{x}_\mathrm{a}\cos\left(\theta_p\right) + m_p l_p^2\ddot{\theta}_p + c_{GB}\dot{\theta}_p + T_{GB} + m_p g l_p\sin\left(\theta_p\right) = -\ddot{x}_g m_p l_p, \tag{15}$$

where T_{GB} is the gearbox output torque; for the pre-yield case, in which $|T_{MR}| \leq T_{MR,y}$, this torque from the loading of the torsional spring:

$$T_{GB} = k_t\left(\frac{N_R}{N_S}\right)^2\left(\theta_p + \theta_{p,y} - \theta_{p,max}\right), \tag{16}$$

and for the post-yield case when $|T_{MR}| > T_{MR,y}$:

$$T_{GB} = T_{MR,y}\,\mathrm{sgn}(\dot{\theta}_p)\left(\frac{N_R}{N_R + N_S}\right). \tag{17}$$

As a final step, to analyse the system, it must be linearized, taking $\sin(\theta_p) = \theta_p$, $\cos(\theta_p) = 1$, and also $\dot{\theta}_p^2 = 0$. **Equations 14 and 15**, then become **Equations 18 and 19**, respectively, first with $q_1 = x_a$:

$$(m_a + m_p)\ddot{x}_\mathrm{a} + m_p l_p \ddot{\theta}_p + c_a \dot{x}_a + k_a x_a = -\ddot{x}_g(m_a + m_p), \tag{18}$$

and for $q_2 = \theta_p$:

$$m_p l_p \ddot{x}_\mathrm{a} + m_p l_p^2 \ddot{\theta}_p + c_{GB}\dot{\theta}_p + T_{GB} + m_p g l_p \theta_p = -\ddot{x}_g m_p l_p, \tag{19}$$

where T_{GB} is defined as in **Equations 16 and 17** for the pre- and post-yield states, respectively.

3.2. Model Validation

To verify the accuracy of the MR-PTMD model in replicating the dynamics of the physical system, the frequency response of the simulated MR-PTMD with a 0 A to 3 A input current range was compared against the experimentally determined response. In the simulation case, the MR-PTMD parameters are as included in Section 2, with the exception of c_a and k_a, which were set to arbitrarily high values, as the structure is assumed to be rigidly coupled to the floor upon which it rests. In both cases, sinusoidal displacement amplitudes of 10 mm through a frequency sweep of 1 Hz to 10 Hz served as the excitation, and the ratio of peak absolute pendulum mass displacement, i.e. $\theta_p l_p$, to peak input excitation x_g was calculated as the transmissibility of the device. The simulated response is included in **Figure 5**, demonstrating variable resonance behaviour which is consistent with the experimental result presented in (Christie et al., 2019), in the simulated case shifting resonant frequency from 2.3 Hz to 4.6 Hz over the 0-3 A current range. As for the decreased transmissibility evident immediately when current is increased above 0 A, this is due to the increase in the equivalent damping coefficient c_{eq} of the damper when the MRF is continuously yielding in the semi-solid state. This contributes greater damping to the TMD, thereby reducing transmissibility. As the damper becomes more rigid, the effect subsides as internal displacement of the damper θ_{MR} eventually approaches zero. The curves then tend to blend together as the torque produced by the damper saturates, hence why the 2.5 A and 3 A results are identical.

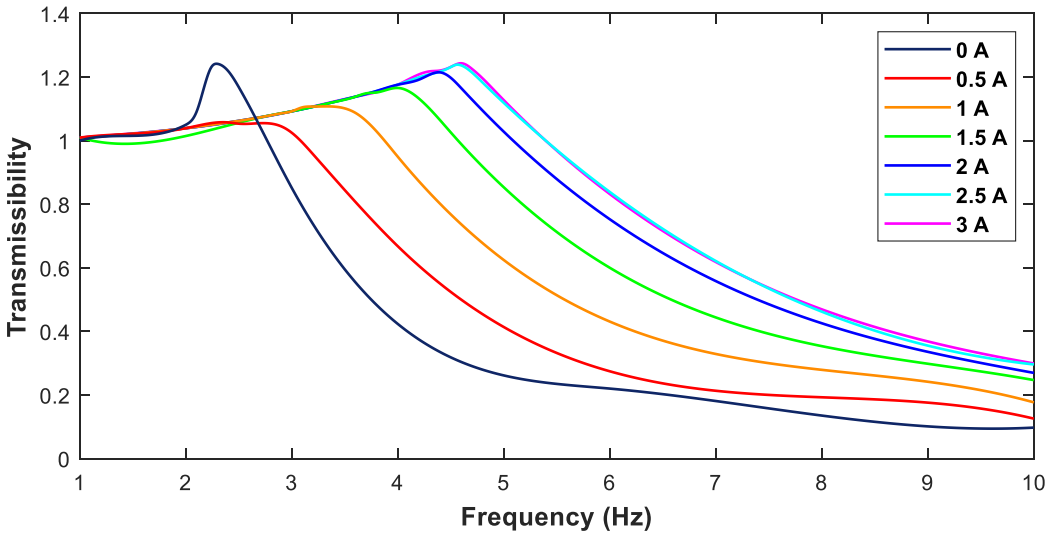

Figure 5 – MR-PTMD simulated frequency response

As plotted in **Figure 6**, the resonant peaks of the simulation are compared against those of the previous experimental results. It is evident that the model is representative of the physical system, with the experimental and simulated resonance-current relationships following a similar trend across the frequency range tested. In both cases, approximately a 100% increase in resonant frequency is observed with low error in between theoretical-based and experimental results, hence validating the model.

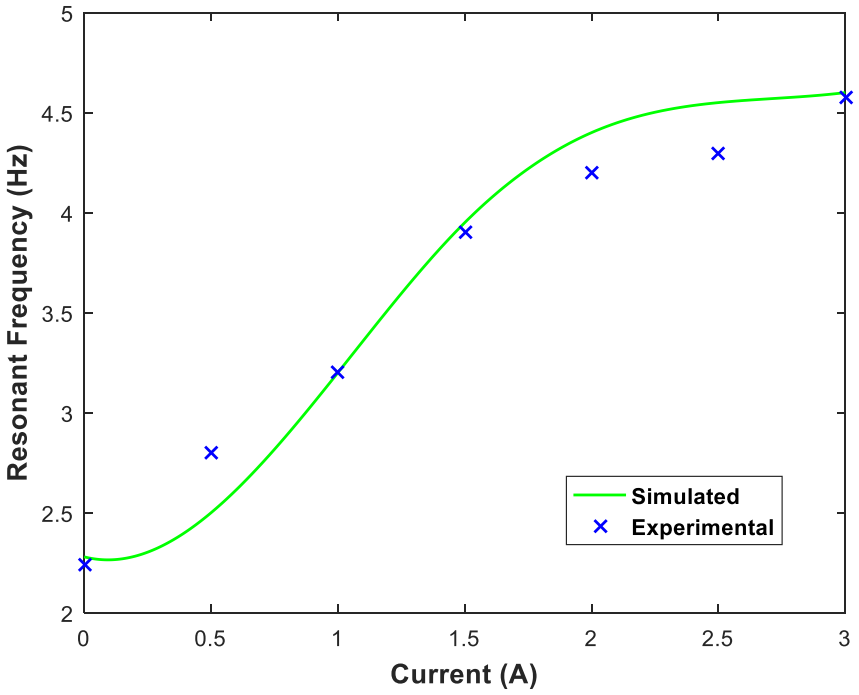

Figure 6 – MR-PTMD simulated and experimental current-resonance behaviour

3.3. Short-time Fourier Transform Control Algorithm

As applied experimentally in (Christie et al., 2019), short-time Fourier transform (STFT) was employed here to facilitate semi-active control of the MR-PTMD through control of damper current I and hence yield torque $T_{MR,y}$. This STFT control yields the dominant frequency of a signal in a specified time-frame. Given the concept applied here is to set the TMD resonance to match the excitation frequency, an optimal damper current can be selected such that the MR-PTMD best attenuates the input vibration for any frequency within its tuneable range. This STFT process is governed by the following equations, **Equations 20-23**, starting with the segmentation of the input signal $x(t)$:

$$x_\tau(t) = x(t)h(t-\tau), \tag{20}$$

where $x_\tau(t)$ is the input signal segment, t is time, and $w(t-\tau)$ is a window function with a fixed window time τ. Fourier transform of the windowed segment of the input is then applied:

$$X_\tau(\omega) = \frac{1}{\sqrt{2\pi}} \int x_\tau(t) e^{-j\omega t}\, \mathrm{d}t, \tag{21}$$

where $X_\tau(\omega)$ is the Fourier transform of the windowed signal, and ω is angular frequency. The energy density spectrum $P(\tau, \omega)$ of this signal for a given window time τ is equal to the square of the Fourier transform in **Equation 21**:

$$P(\tau, \omega) = |X_\tau(\omega)|^2. \tag{22}$$

From this definition, the instantaneous dominant frequency $\langle \omega_\tau \rangle$ can be found from:

$$\langle \omega_\tau \rangle = \frac{1}{|x(\tau)|^2} \int \omega P(\tau, \omega)\, \mathrm{d}\omega. \tag{23}$$

Based on this knowledge of live excitation dominant frequency $f = \omega/2\pi$, a simple mapping of damper input current I to TMD resonance frequency $f_n = f$ can complete this control regime when coupled with **Equations 1-5**. Inverting the simulated curve plotted in **Figure 6** and applying a cubic fit yields the following frequency-to-current mapping curve:

$$I(f) = 0.4855f^3 - 4.7813f^2 + 16.076f - 17.376, \tag{24}$$

where the current will saturate at the functional limits of the device, resulting in an output of 0 A when $f < 2.3$ Hz and 3 A when $f > 4.6$ Hz. This facilitates resonance tracking of input

excitation within this bandwidth to provide minimum transmissibility of the 5th floor of the scale building in subsequent seismic excitation experiments.

Consequent from the window time and size of this STFT-based control, however, is a time delay in the control effort. While a larger window time and hence smaller window size results in greater frequency fidelity, this also leads to a slower response time in the control current supplied to the MR-PTMD. The controller parameters were heuristically tuned prior to seismic excitation tests, with a measured time delay of up to ~500 ms. This tuning was performed with the goal of optimal average performance across the later evaluation indices of floor displacement and acceleration, as discussed further in Section 4.2.

4. Scale-Building Experimental Studies

4.1. Scale-Building Experimental Setup

As included in the studies presented in (Christie et al., 2019), a scale 5-story building was constructed to evaluate the prototype MR-PTMD's seismic protection performance when attached to the top floor of a building. Illustrated in the shaker-table experimental setup of **Figure 7**, this building was based on a ~20 m tall building, using a 1:20 length scale. Following dimensional scaling laws, this leads to a floor spacing of 180 mm, and via. the respective mass scale of 1:20^3, a mass of 5.0 kg (including floor self-weight and payload). To excite the building with seismic records, a 6-DOF linear-actuator-based shaker platform was used to translate along a single axis. To investigate the response of the building, two accelerometers (ADXL 203EB) were used to collect floor acceleration and a laser displacement sensor (Micro-Epsilon ILD1302-100) was used to collect floor displacement relative to the ground level (shaker table), with the laser supported on a column fixed to the table. Several iterations of each test run, i.e. a given earthquake and TMD control mode, were carried out, moving the displacement laser and floor accelerometer along to collect data for each floor. To log data, a DAQ (NI cDAQ-9174 with NI 9201 module) was employed. This DAQ was used in conjunction with an NI myRIO-1900 to facilitate real-time control, performing the aforementioned STFT analysis on the top-floor acceleration to output a control signal to the MR-PTMD.

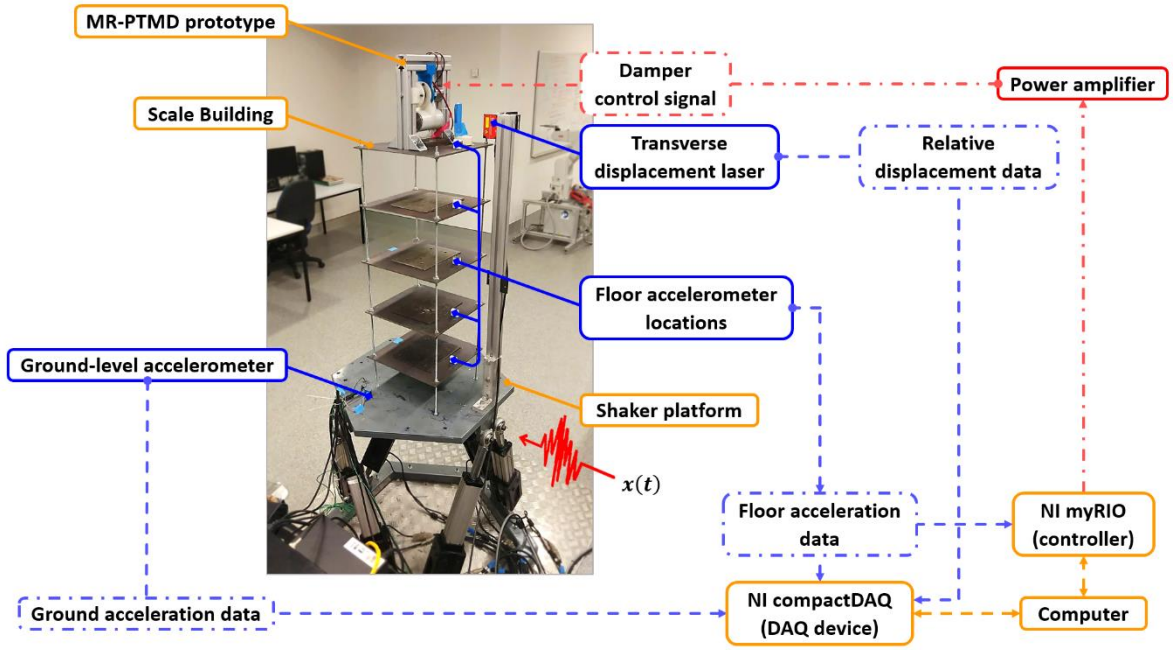

Figure 7 – Scale 5-story building experimental setup

4.2. Seismic Vibration Testing

To investigate the MR-PTMD's seismic vibration suppression performance, in extension to the 1994 Northridge record included in (Christie et al., 2019), the 1940 El Centro and 1985 Mexico City earthquakes were used as benchmarks for this case-study. Given the two records possess relatively high and low dominant frequencies, respectively, they are able to demonstrate the versatility of the MR-PTMD through semi-active control. Both of these records were adjusted according to a 1:4 timescale, following from the scale-building length scale. For both of these records, relative displacement and acceleration data were collected for each floor for three test cases: passive-off (0 A damper current), passive-on (1.8 A damper current), and semi-active (STFT) control. It should also be mentioned that in previous studies, optimal vibration absorption was found to occur when damper current was set to 1.8 A, matching the TMD's resonance to that of the 5th floor of the scale-building.

To demonstrate the displacement and acceleration response of the building under the two earthquake records and different control methods, representative 5th floor time-trace data has been included in **Figure 8 and 9**. Qualitatively, it can be quite clearly observed in the El Centro response of **Figure 8(a)** that the RMS displacement of the 5th floor with the passive-off TMD tuning is greater than both the passive-on and semi-active cases, with similar behaviour visible in the acceleration data of **Figure 8(b)**. These two cases for the 5th floor represent a 23.61% and 15.05% reduction over the passive-off case, respectively, however with similar performance to

the passive-on case here. On the other hand, **Figure 9** shows the opposite behaviour; for the Mexico City event, the passive-on performance appears to be the worst of the three cases, particularly in regards to peak displacement and acceleration. Here, it observed that for the 5th floor, semi-active control of the MR-PTMD leads to a 13.40% reduction in peak relative displacement, along with a reduction in peak acceleration of 28.09%. This is now in contrast to the El Centro case, where the semi-active device performed similar to passive-on case to achieve an optimal result. What this result highlights is that for seismic events with shifted frequency spectrums, passive-optimal tuning may in fact not be adequate, or, at least, may offer sub-par performance. As an alternative, semi-active STFT-based control of this MR-PTMD can adjust the resonance of the device to attain optimal performance in a range of cases.

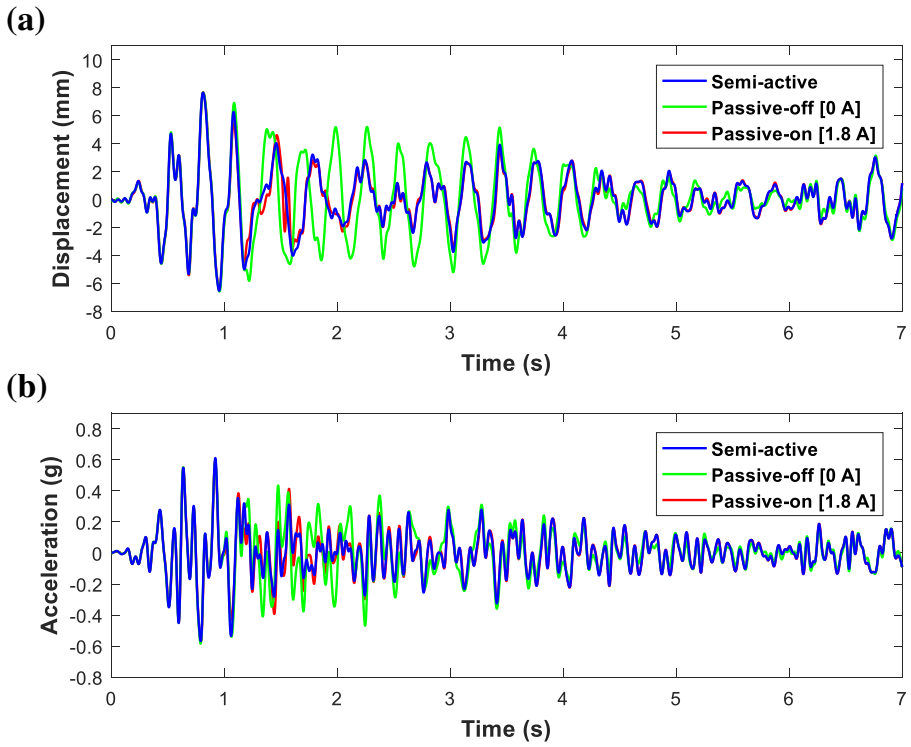

Figure 8 – Scale building 5th floor (a) relative displacement, and (b) acceleration response under El Centro earthquake excitation

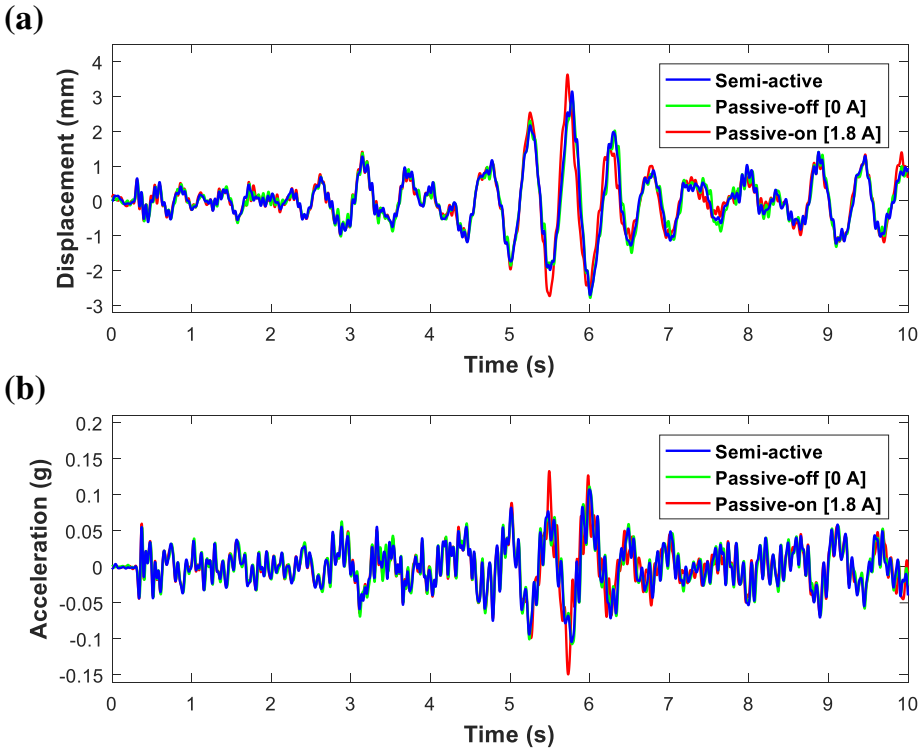

Figure 9 – Scale building 5th floor (a) relative displacement, and (b) acceleration response under Mexico City earthquake excitation

To further analyse the seismic response of the building, data collected for each floor has been processed into: peak relative displacement, RMS relative displacement, peak acceleration, and RMS acceleration. For the El Centro case, the relative displacement data is presented in **Figure 10**, with tabulated values included in **Table 1**, and the acceleration data is presented in **Figure 11**, with the numerical data in **Table 2**. The interesting observation that can be made for the displacement trend across floors is that, as seen in **Figure 10(a)**, regardless of the control case, peak magnitudes are quite similar with the increased amplitude of floor 2 for the passive-off case being the only major exception to an otherwise linear trend with increasing floor number. As indicated from the time-trace of **Figure 8(a)** earlier, the RMS relative displacement of **Figure 10(b)** is quite apparently higher for the passive-off case across all floors, with a maximum RMS displacement of 2.47 mm, in contrast to the 1.89 mm (23.61% reduction) of the semi-active case.

From the acceleration data of **Figure 11** and **Table 2** for the El Centro tests, the complex resonance mode shapes of the structure become apparent. This point notwithstanding, in **Figure 11(a)**, the semi-active controlled case shows good reduction in peak acceleration consistently across all floors, differing from the passive cases that suffer a more-obvious trade-off at different levels throughout the building. While in some floors the RMS acceleration response of the semi-

active case is not ideal, with the passive-on case performing quite well in **Figure 11(b)**, the semi-active case still represents a reduction from the alternative passive-off case as high as 21.90% for the 4th floor, followed by a 15.05% reduction for the 5th floor.

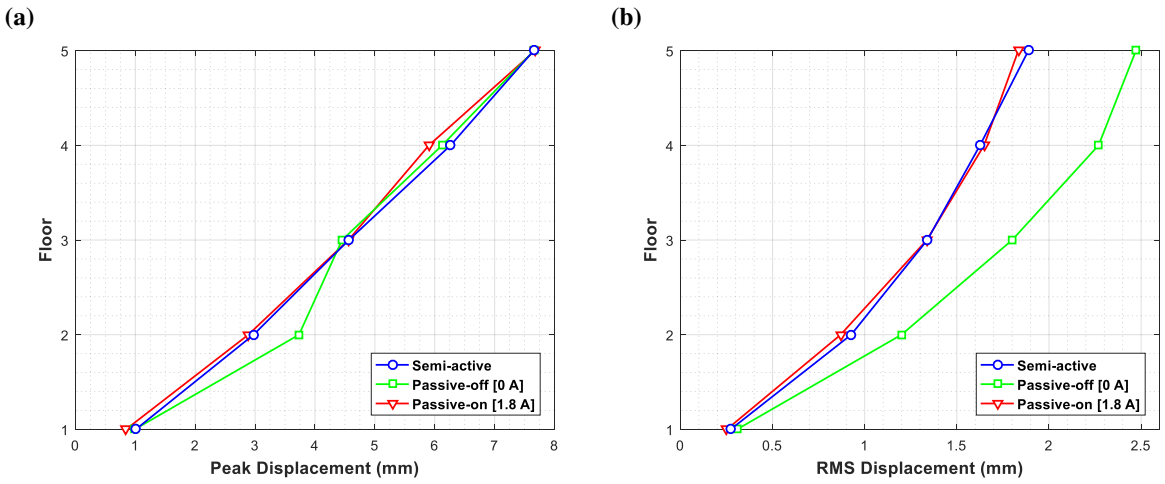

Figure 10 – El Centro excitation scale-building relative displacement (a) peak, and (b) RMS response

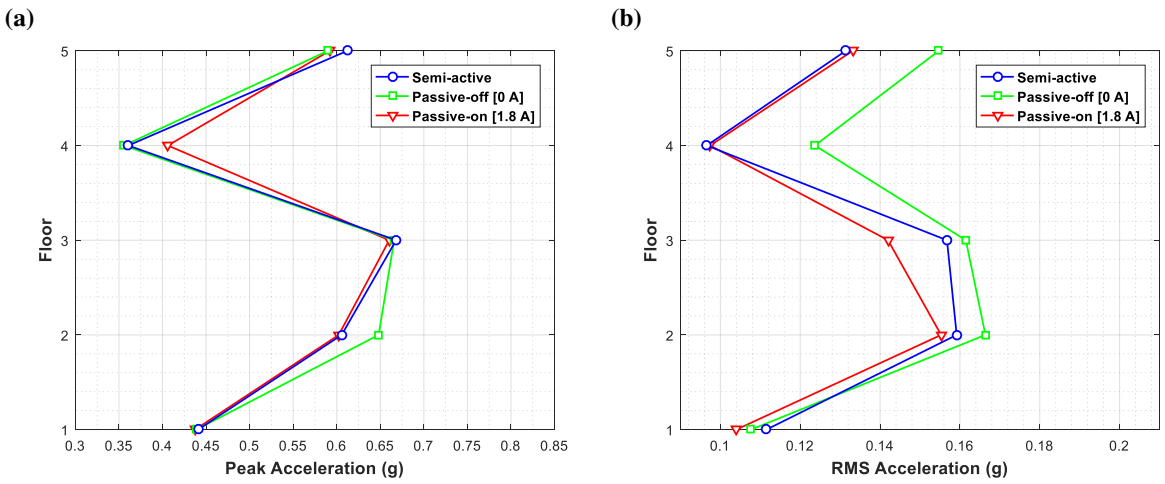

Figure 11 – El Centro excitation scale-building acceleration (a) peak, and (b) RMS response

Table 1 – El Centro experimental peak and RMS relative displacement data

	Peak relative displacement (mm)				
Floor	**Passive-off tuning**	**Passive-on tuning**	**Semi-active control**		
			Mag.	**% reduction (rel. passive-off)**	**% reduction (rel. passive-on)**
1	0.9881	0.8430	1.0068	-1.89%	-19.44%
2	3.7328	2.8868	2.9735	20.34%	-3.00%
3	4.4523	4.5586	4.5656	-2.54%	-0.15%
4	6.1225	5.9027	6.2635	-2.30%	-6.11%
5	7.6583	7.6760	7.6522	0.08%	0.31%
	RMS relative displacement (mm)				
1	0.3065	0.2511	0.2722	11.18%	-8.41%
2	1.1994	0.8693	0.9263	22.77%	-6.55%
3	1.8002	1.3368	1.3397	25.58%	-0.22%
4	2.2689	1.6477	1.6255	28.36%	1.35%
5	2.4719	1.8336	1.8883	23.61%	-2.98%

Table 2 – El Centro experimental peak and RMS acceleration data

	Peak acceleration (g)				
Floor	**Passive-off tuning**	**Passive-on tuning**	**Semi-active control**		
			Mag.	**% reduction (rel. passive-off)**	**% reduction (rel. passive-on)**
1	0.4389	0.4373	0.4408	-0.45%	-0.80%
2	0.6481	0.6023	0.6056	6.56%	-0.55%
3	0.6659	0.6603	0.6681	-0.34%	-1.19%
4	0.3557	0.4061	0.3607	-1.40%	11.19%
5	0.5899	0.5919	0.6122	-3.77%	-3.43%
	RMS acceleration (g)				
1	0.1077	0.1040	0.1115	-3.56%	-7.25%
2	0.1664	0.1553	0.1592	4.32%	-2.51%
3	0.1615	0.1420	0.1568	2.93%	-10.39%
4	0.1237	0.0974	0.0966	21.90%	0.87%
5	0.1547	0.1331	0.1314	15.05%	1.30%

Regarding the 1985 Mexico City earthquake response, as briefly discussed, the general performance of the passive-on case, which should be optimal for this building, cannot even yield the level of performance the passive-off case achieves, with this being reflected in both the displacement response of **Figure 12** and **Table 3**, and also the acceleration response included in **Figure 13** and **Table 4**. Also seen in the RMS response, but particularly in the peak relative

displacement of **Figure 12(a)** and peak acceleration of **Figure 13(a)**, the semi-active controlled device has comparable performance to the low-resonance passive-off tuning, with the high-resonance passive-on tuning exacerbating building vibration. In terms of representative peak reduction from the passive-on device, the semi-active case resulted in a 13.40% and 28.09% reduction in 5th floor displacement and acceleration, respectively. This is due to the necessity of a variable TMD resonance, as passive tunings only perform well with a very limited bandwidth, in contrast to higher-bandwidth devices, namely those which possess variable resonance.

Between the two seismic excitation cases, it should be noted that the semi-active control mode cannot guarantee optimal performance across all floors for each test metric, as indicated in the experimental results for some floors. While it is demonstrated that the semi-active control provides more versatile performance when managing varying frequency spectra of different seismic records, alternative semi-active control regimes may further improve performance for this system. For example, robust controllers such as H_2 and H_∞ have been demonstrated to be effective in vibration reduction performance overall across all floors of scale-buildings excited by seismic records (Yoshioka; Arash Yeganeh and Touraj, 2014). However, these require model uncertainties to be closely managed, as opposed to the relatively simple implementation of STFT-based control included here. Modern research in this field has further shown benefits in applying neural network (NN) learning models (Gu et al., 2017).

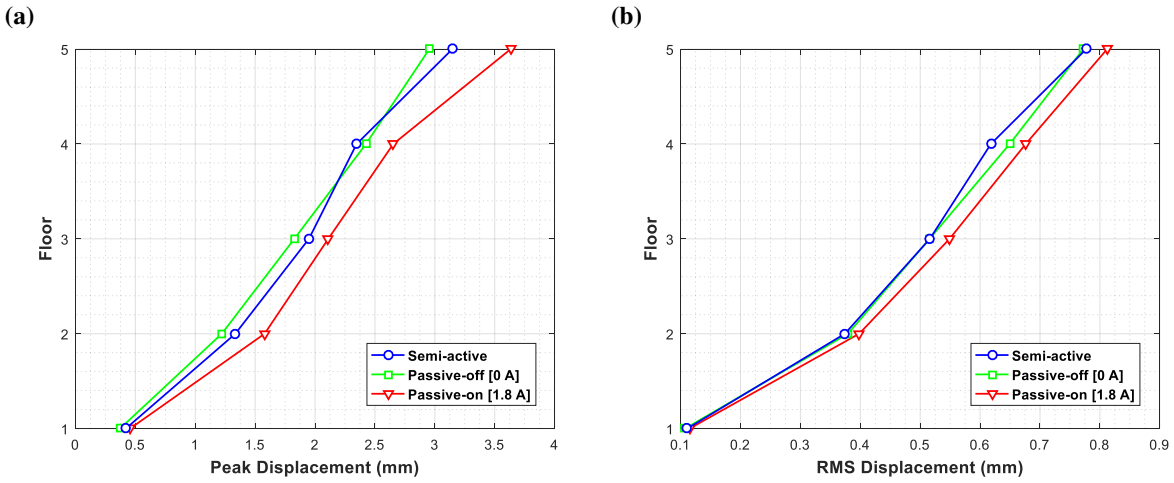

Figure 12 – Mexico City excitation scale-building relative displacement (a) peak, and (b) RMS response

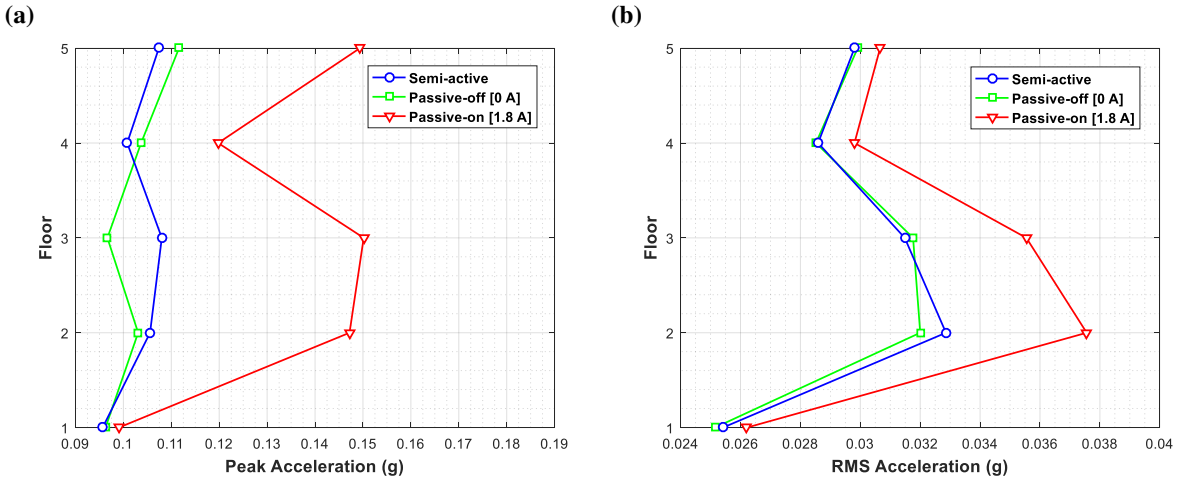

Figure 13 – Mexico City excitation scale-building acceleration (a) peak, and (b) RMS response

Table 3 – Mexico City experimental peak and RMS relative displacement data

	Peak relative displacement (mm)				
Floor	**Passive-off tuning**	**Passive-on tuning**	**Semi-active control**		
			Mag.	**% reduction (rel. passive-off)**	**% reduction (rel. passive-on)**
1	0.3716	0.4557	0.4201	-13.05%	7.81%
2	1.2215	1.5789	1.3346	-9.26%	15.47%
3	1.8268	2.1104	1.9487	-6.68%	7.66%
4	2.4248	2.6530	2.3469	3.21%	11.54%
5	2.9537	3.6329	3.1463	-6.52%	13.40%
	RMS relative displacement (mm)				
1	0.1072	0.1148	0.1109	-3.47%	3.36%
2	0.3793	0.3981	0.3743	1.34%	5.99%
3	0.5156	0.5490	0.5161	-0.09%	6.00%
4	0.6493	0.6761	0.6180	4.83%	8.60%
5	0.7722	0.8121	0.7772	-0.64%	4.30%

Table 4 – Mexico City experimental peak and RMS acceleration data

	Peak acceleration (g)				
Floor	**Passive-off tuning**	**Passive-on tuning**	**Semi-active control**		
			Mag.	**% reduction (rel. passive-off)**	**% reduction (rel. passive-on)**
1	0.0963	0.0990	0.0957	0.63%	3.40%
2	0.1031	0.1472	0.1056	-2.41%	28.28%
3	0.0967	0.1502	0.1080	-11.74%	28.06%
4	0.1037	0.1198	0.1008	2.80%	15.85%
5	0.1116	0.1494	0.1074	3.77%	28.09%
	RMS acceleration (g)				
1	0.0251	0.0262	0.0254	-1.05%	3.03%
2	0.0320	0.0376	0.0329	-2.69%	12.51%
3	0.0318	0.0355	0.0315	0.88%	11.42%
4	0.0285	0.0298	0.0286	-0.25%	4.07%
5	0.0299	0.0307	0.0298	0.35%	2.79%

5. Conclusions

The MR-damper-controlled variable resonance pendulum tuned mass damper, the MR-PTMD was analytically investigated with a comprehensive mathematical model derived and validated against experimental data. Furthermore, to experimentally investigate the performance of the device, two seismic records were employed as performance benchmarks in the devices capability in suppressing building vibration. Through passive and semi-active control modes, the MR-PTMD was shown to be effective and versatile in seismic vibration suppression of a multi-story building, particularly through STFT semi-active control. Consequently, the semi-active device showed the most substantial improvement over the passive-off tuning for the El Centro earthquake, at best reducing RMS displacement and acceleration by 28.36% and 21.90%, respectively. Where the semi-active device performed better in the Mexico City case was over the passive-on tuning, at best reducing peak displacement by 15.47% and acceleration by 28.28%. In both cases, conventional passive tuning was demonstrated to be an issue for managing different seismic events with dissimilar frequency spectrums, however, the semi-active controlled MR-PTMD was able to adapt, attributed to its variable resonance behaviour.

Acknowledgements

This research is supported by the Australian Research Council Discovery Grants (No. DP150102636 and LP150100040), National Natural Science Foundation of China (No. 51375468), and has been conducted with the support of the Australian Government Research Training Program Scholarship.

References

Altay O and Klinkel S. (2018) A semi-active tuned liquid column damper for lateral vibration control of high-rise structures: Theory and experimental verification. *Structural control and health monitoring* 25: e2270.

Arash Yeganeh F and Touraj T. (2014) Robust semi-active control for uncertain structures and smart dampers. *Smart Materials and Structures* 23: 095040.

Buckle IG and Mayes RL. (1990) Seismic Isolation: History, Application, and Performance—A World View. *Earthquake Spectra* 6: 161-201.

Christie MD, Sun S, Deng L, et al. (2019) A variable resonance magnetorheological-fluid-based pendulum tuned mass damper for seismic vibration suppression. *Mechanical Systems and Signal Processing* 116: 530-544.

LORD Co. (2008) *LORD TECHNICAL DATA: MRF-140CG Magneto-Rheological Fluid*. Available at: http://www.lordfulfillment.com/upload/DS7012.pdf.

de Vicente J. (2011) Magnetorheological fluids: a review. *Soft matter* 7: 3701-3710.

Fisco NR and Adeli H. (2011) Smart structures: Part II - Hybrid control systems and control strategies. *Scientia Iranica* 18: 285-295.

Gu X, Yu Y, Li J, et al. (2017) Semi-active control of magnetorheological elastomer base isolation system utilising learning-based inverse model. *Journal of Sound and Vibration* 406: 346-362.

Gutierrez Soto M and Adeli H. (2013) Tuned Mass Dampers. *Archives of computational methods in engineering* 20: 419-431.

Harris BJ, Sun SS and Li WH. (2017) Improving stability and curving passing performance for railway vehicles with a variable stiffness MRF rubber joint. *Smart Materials and Structures* 26.

Hoang N. (2008) Optimal tuned mass damper for seismic applications and practical design formulas. *Engineering structures* 30: 707-715.

Imaduddin F, Mazlan SA and Zamzuri H. (2013) A design and modelling review of rotary magnetorheological damper. *Materials & Design* 51: 575-591.

Jain VK. (2008) Abrasive-Based Nano-Finishing Techniques: An Overview. *Machining Science and Technology* 12: 257-294.

Jha S and Jain VK. (2004) Design and development of the magnetorheological abrasive flow finishing (MRAFF) process. *International Journal of Machine Tools and Manufacture* 44: 1019-1029.

Kela L. (2009) Recent Studies of Adaptive Tuned Vibration Absorbers/Neutralizers. *Applied mechanics reviews* 62: 060801-060809.

Lourenco R. (2011) *Design, construction and testing of an adaptive pendulum tuned mass damper*. MA Thesis, University of Waterloo, US

Sun S, Deng H, Du H, et al. (2015) A Compact Variable Stiffness and Damping Shock Absorber for Vehicle Suspension. *IEEE/ASME Transactions on Mechatronics* 20: 2621-2629.

Sun S, Deng H, Yang J, et al. (2015) An adaptive tuned vibration absorber based on multilayered MR elastomers. *Smart Materials and Structures* 24.

Sun S, Yang J, Du H, et al. (2018) Development of magnetorheological elastomers–based tuned mass damper for building protection from seismic events. *Journal of Intelligent Material Systems and Structures*: 1045389X17754265.

Tang X. (2017) Takagi–Sugeno Fuzzy Control for Semi-Active Vehicle Suspension With a Magnetorheological Damper and Experimental Validation. *IEEE/ASME Transactions on Mechatronics* 22: 291-300.

Yang J, Sun S, Tian T, et al. (2016) Development of a novel multi-layer MRE isolator for suppression of building vibrations under seismic events. *Mechanical Systems and Signal Processing* 70–71: 811-820.

Yao Z, Mei D and Chen Z. (2011) Chatter suppression by parametric excitation: Model and experiments. *Journal of Sound and Vibration* 330: 2995-3005.

Yoshioka H, Ramallo JC and Spencer BF. (2002) "Smart" Base Isolation Strategies Employing Magnetorheological Dampers. *Journal of Engineering Mechanics* 128: 540-551.

Zhang S and Wang G. (2013) Effects of near-fault and far-fault ground motions on nonlinear dynamic response and seismic damage of concrete gravity dams. *Soil Dynamics and Earthquake Engineering* 53: 217-229.

Zhou Y, Li W and Hadi M. (2010) Performance comparison between an MRF damper and an MRE isolator incorporated with a building structure. *Applied Mechanics and Materials.* 862-865.